Impact of the Fluid Flow Conditions on the Formation Rate of Carbon Dioxide Hydrates in a Semi-Batch Stirred Tank Reactor

S. Douïeb
URPEI, Dept. of Chemical Engineering, École Polytechnique de Montréal, Station CV, Montreal, H3C 3A7, Canada

TIPs, Université Libre de Bruxelles, Av. F.D. Roosevelt 50, CP 165/67, 1050 Brussels, Belgium

L. Fradette and F. Bertrand
URPEI, Dept. of Chemical Engineering, École Polytechnique de Montréal, Station CV, Montreal, H3C 3A7, Canada

B. Haut
TIPs, Université Libre de Bruxelles, Av. F.D. Roosevelt 50, CP 165/67, 1050 Brussels, Belgium

DOI 10.1002/aic.14952
Published online July 26, 2015 in Wiley Online Library (wileyonlinelibrary.com)

CO_2 hydrate formation experiments are performed in a 20 L semi-batch stirred tank reactor using three different impellers (a down-pumping pitched blade turbine, a Maxblend™, and a Dispersimax™) at various rotational speeds to examine the impact of the flow conditions on the CO_2 hydrate formation rate. An original mathematical model of the CO_2 hydrate formation process that assigns a resistance to each of its constitutive steps is established. For each experimental condition, the formation rate is measured and the rate-limiting step is determined on the basis of the respective values of the resistances. The efficiencies of the three considered impellers are compared and, for each impeller, the influence of the rotational speed on the rate-limiting step is discussed. For instance, it is shown that a formation rate limitation due to heat transfer can occur at the relatively small scale used to perform our experiments. © 2015 American Institute of Chemical Engineers *AIChE J*, 61: 4387–4401, 2015

Keywords: hydrates, mixing, crystal growth (industrial crystallization), mathematical modeling, heat transfer

Introduction

Carbon dioxide (CO_2) capture and storage (CCS) has become a major research focus due to the potential of CCS for mitigating anthropogenic CO_2 emissions. CCS is aimed at large point emission sources such as fossil fuel power plants and major industrial CO_2-emitters such as cement kiln plants and refineries. In this method, CO_2 is first separated ("captured") from flue/fuel gases, transported and then either isolated from the atmosphere in a long-term storage location or used industrially.[1,2] Reducing the cost of separation, which is the principal financial impediment to CCS projects, is one of the main challenges to making industrial CCS deployment economically feasible.[1–3] Conventional separation technologies based on chemical absorption, physical adsorption, membrane separation, and cryogenic distillation are very energy intensive and suffer from other drawbacks such as chemical degradation, low capacity, or high capital costs.[1,4–6]

Hydrate-based CO_2 separation (HBCS) techniques have been receiving increasing attention as promising viable alternatives to conventional capture technologies.[1,4,7] In these techniques, flue/fuel gases containing CO_2 are exposed to liquid water under high pressure, resulting in the formation of CO_2 hydrates. Gas hydrates are ice-like solid compounds in which gas molecules are physically trapped by van der Waals forces in polyhedral cages formed by hydrogen-bonded water molecules.[8] Gases that form hydrates when they come into contact with liquid water at the appropriate temperature (typically less than 300 K) and pressure (typically more than 0.6 MPa) are small molecules (< 0.9 nm), including light hydrocarbon gases such as methane and CO_2, rare gases such as argon and krypton, and diatomic gases such as nitrogen and oxygen.[9] The basis of CO_2 separation by gas hydrate formation is that, when a flue/fuel gas is put in contact with liquid water in conditions leading to the formation of hydrates, CO_2 is preferentially incorporated into the cages of the formed hydrates, compared with the other molecules of the gas. This results in a CO_2-rich hydrate phase and a CO_2-poor residual gas phase.[3,4] This formation, taking place within the liquid water phase, can be described as a crystallization in solution process that involves a series of mass and heat transfer steps.[10]

Relative to the other separation techniques, the advantages of HBCS techniques are the high storage capacity, low investment, small energy penalty, simple process, and environmental friendliness.[4,11,12] Furthermore, the decomposition of the

Additional Supporting Information may be found in the online version of this article.

Correspondence concerning this article should be addressed to L. Fradette at louis.fradette@polymtl.ca

hydrates generates CO_2 at elevated pressure, which reduced the compression costs associated to the downstream CCS steps (transport, storage, or sequestration).[12,13] Last, gas hydrates have also been considered as a potential means for deep ocean storage of CO_2.[14,15] Nonetheless, several factors make that HBCS is still in the research stage. First, this technology is relatively recent comparatively to the established CO_2 separation technologies. Additional efforts have to be made in the acquisition and modeling of phase equilibrium data for CO_2-other gas(es)-in-water[8,16–18] and intrinsic kinetics data relative to the formation of hydrate from such systems.[3,19–22] These information are of fundamental importance for the design of separation processes utilizing gas hydrate formation. Second, CO_2 hydrate formation typically requires high pressure, especially if the CO_2 concentration in the hydrate-forming gas mixture is low, which can lead to prohibitive operating costs related to the compression of the gas to the necessary hydrate formation pressure. This fact is currently limiting the interest of the application of HBCS for the treatment of flue gases (post-combustion CO_2 capture), in which the CO_2 concentration is typically low (~10–20 mol %).[11,12] However, it is believed that HBSC would be more competitive than conventional capture technologies for the treatment of fuel gases from gasification plants (pre-combustion capture), generally called "synthesis gas" or "syngas," in which the CO_2 concentration can be much higher.[11,12,23] For example, a syngas that has undergone a water gas shift reaction typically has a CO_2 concentration on the order of 40 mol % (the rest of the gas being principally composed of H_2) and comes out of the water gas shift converter at relatively high pressure, which is advantageous for hydrate formation.[11,12] Finally, the capability of HBCS techniques to process the important amount of CO_2 involved in CCS applications with a sufficient productivity has yet to be established.[4,11,22]

In order to contribute to the transfer of HBCS techniques from the laboratory benches to industrial scale applications such as CCS, there is an ongoing search for strategies that would enable to generate CO_2 hydrates at low operating costs and with a high productivity. Two approaches are receiving the most attention. The first is the development of chemical additives that can moderate the CO_2 hydrate formation conditions (thermodynamic additives) or promote their rate of formation (kinetic additives). Although, to date, no stand-out additives have been identified, some thermodynamic additives, such as tetra-*n*-butyl ammonium fluoride, cyclopentane, tetrahydrofuran, and tetra-*n*-butyl ammonium bromide, and some kinetic additives, such as sodium dodecyl sulfate, have demonstrated their ability to considerably reduce the equilibrium hydrate formation pressure and substantially promote the hydrate formation rate, respectively.[12,22–27] The second approach is the development of apparatuses specifically designed to generate gas hydrates with a high productivity.[28–30] A great effort is being made to find efficient contacting mode between the gas, liquid, and solid phases in terms of mass and heat transfer performances.[4,12] The apparatuses developed generally resort to bubbling, spraying, and stirring.[29–34] Another point of focus is the development of apparatuses that operate in continuous mode.[4] While no compelling breakthrough apparatus design has yet emerged, several advanced pilot scale reactors, recently developed by different groups, have demonstrated their capability to produce CO_2 hydrate at high rate for extended periods of time and their potential for scalability. For example, Szymcek et al.[35] developed a continuous jet hydrate reactor, that contacts CO_2 and water using a multiple capillary injector system and extrudes hydrate solid particles. Another example is the tubular continuous flow reactor designed by Yang et al.,[7] that consists of a Venturi gas-liquid mixer followed by several tubular finned heat exchangers.

The most straightforward and economic method used in chemical engineering to increase the rate at which a given process involving mass and heat transfers takes place is to carry it out in the presence of a flow field. Surprisingly, no extensive study on the effect of the flow conditions on the formation rate of gas hydrates has been performed. A great number of gas hydrate formation studies have been carried out with mechanical agitation or under flowing conditions, and several have shown that an increase in mixing intensity results in an increase in the formation rate.[10,13,21,36–41] However, the results from these studies with respect to the effect of the flow conditions on the gas hydrate formation rate are of limited use for the design of efficient large-scale reactors. More often than not, the experimental setups used in these studies consist in small-agitated vessels in which the liquid volume almost never exceeds 1 L. Such small volumes do not reflect the various limitations, especially heat transfer, that are typically encountered with industrial size reactors. Furthermore, the results of these studies are almost always reported in terms of the effect of a unique fluid flow-related parameter, generally only linked to the mixing intensity and specific to the setup used (such as the rotational speed of a given impeller or the fluid velocity), on the global hydrate formation rate. This fact makes it difficult to identify general flow characteristics that lead to high formation rate. Moreover, it does not allow determining neither which steps of the CO_2 hydrate formation process are particularly influenced by these characteristics nor the extent of these influences. Consequently, these studies do not allow drawing general conclusions that could be applied to design and optimize the flow conditions of other systems or scales.

The general objective of this work is to characterize the impact of the flow conditions on the CO_2 hydrate formation rate. For this purpose, several CO_2 hydrate formation experiments are performed under different flow conditions using a medium-sized (20 L) semi-batch stirred tank reactor. Stirred tanks, in addition to being used for industrial applications, are well suited for studies requiring different flow conditions. To generate various flow conditions, two fluid flow-related parameters are varied. First, different rotational speeds of the impeller are used. Second, three different impellers are used: a down-pumping pitched blade turbine (PBTD), a Maxblend™, and a Dispersimax™. The impact of the flow conditions generated by the impellers on the CO_2 hydrate formation rate is characterized based on their effect on two variables: the magnitude of the formation rate and the nature of the rate-limiting step. The CO_2 hydrate formation rate is measured directly. The nature of the rate-limiting step is identified using two methods. The first is based on an original mathematical representation of the CO_2 hydrate formation process that assigns a resistance to each of its constitutive steps, including those related to heat transfer that are generally not taken into consideration in studies using small reactors. The rate-limiting step is determined by comparing the respective values of the resistances, evaluated experimentally. For the second method, the rate-limiting step is determined by comparing the actual temperature-concentration position of the bulk of the liquid phase during a hydrate formation experiment in the relevant

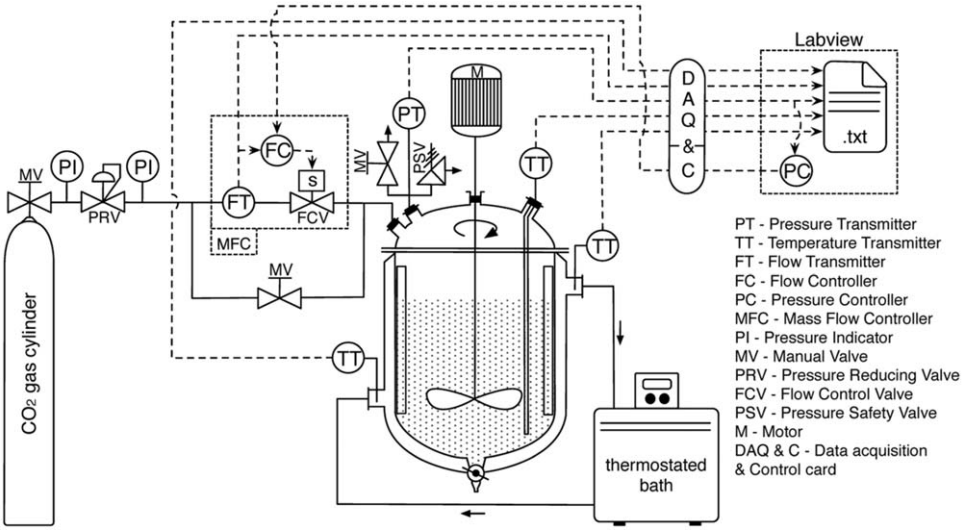

Figure 1. Schematic diagram of the experimental equipment.

isobaric CO_2-in-water solubility diagram, with those corresponding to different limiting cases in which the CO_2 hydrate formation rate is solely limited by one of the constitutive steps of the hydrate formation process.

Experimental Method

Experimental equipment

A schematic diagram of the experimental equipment used to perform the CO_2 hydrate formation experiments is shown in Figure 1. These experiments are carried out in a jacketed stirred tank reactor (Parker Autoclave Engineers Inc.) equipped with an agitator shaft on which various types of impellers can be mounted. The tank has a standard configuration. First, it has a cylindrical shape and a 2:1 elliptical bottom. Second, it has four plate baffles vertically mounted at the tank wall, uniformly spaced and extending from the tank bottom to above the liquid surface. Finally, it is characterized by the following geometrical relationships: $D = H$, $d = D/3$ *or* $D/2$, $W_b = D/12$, where D (m) is the tank inner diameter, H (m) is the liquid height, d (m) is the impeller diameter and W_b (m) is the baffle width. The tank has inner diameter of 0.3 m and a total volume of 38 L. For all the experiments, the tank is filled with 20 L of distilled water in order to ensure that $D = H$. All the parts of the tank in contact with its content are made of 316 stainless steel. The reactor is designed to operate at pressures up to 7.0 MPa and temperatures up to 350°C. The volume of the tank jacket is 7 L. A gas cylinder is used to supply the tank with pressurized CO_2 (>99.8% purity, Air liquide). An electrical motor coupled to a variable speed controller (Altivar-5 series 45-2, Telemecanique) is used to adjust the rotational speed of the agitator shaft up to a maximum speed of 700 rpm. A thermostated circulating bath (model 6506, Polyscience) is used to pump a heat transfer fluid consisting of a mixture of ethylene glycol and water (50/50, V/V) through the tank jacket at a constant flow rate (approximately 15 L/min) and at a temperature ranging from −10°C to 40°C. The thermostated circulating bath is used with its built-in internal temperature probe and is therefore controlling the temperature of the heat transfer fluid at the inlet of the tank jacket.

The temperature of the bulk of the liquid phase is measured using a thermistor (model ON-401-PP-V, ± 0.1°C between 0 and 70°C, Omega Engineering) inserted in a built-in closed-end tube thermowell whose extremity is close to the bottom of the tank. The temperatures of the heat transfer fluid at the inlet and outlet of the jacket are also measured using thermistors (model ON-403-PP, ± 0.1°C between 0 and 70°C, Omega Engineering). The pressure of the gas phase in the tank is measured using a pressure transducer (model AB/HP, 0–7.0 MPa, ± 0.25% span, Honeywell). A mass flow controller (MFC, model GFCS-010509, CO_2 0–22.7 STD L/min, ± 1% span, Aalborg) is used to keep the pressure in the tank constant during the hydrate formation experiments. The mass flow rate measured by the MFC is used to calculate the number of moles of CO_2 supplied to the tank. A data acquisition and control card (SCB-68 connector block + PCI-MIO-16E-1 data acquisition board, National Instruments) connected to a personal computer and controlled by Labview 5.1 software (National Instruments) is used to record the data collected by the different instruments. The card is also used to send the set point commands to the MFC using data received from the pressure transducer and using a built-in PID function in Labview (PC in Figure 1). A bypass line equipped with a manual valve is installed around the MFC to make it possible to rapidly pressurize the tank at the beginning of the experiments. The tank is also equipped with a purge valve and a pressure safety valve.

In addition to varying the rotational speed of the impeller, three different impellers were used to generate different flow conditions inside the tank: a PBTD, a "Maxblend™" (Sumitomo Heavy Industries Process Equipment Co.), and a "Dispersimax™" (Parker Autoclave Engineers Inc.). Schematics of the three impellers are presented in Figure 2.

The PBTD is a traditional turbine impeller widely used to mix low to medium viscosity liquids and suspend solids as well as in heat transfer applications.[42] It provides a combination of both radial and axial flow and generates high shear levels.[42] The Maxblend is a less commonly used impeller composed of a large bottom paddle and an upper grid. It has the particularity to operate efficiently with low to relatively high viscosity fluids[43] and has been observed to generate better pumping[44,45] and solid dispersion[46] than usual impeller configurations. It has also demonstrated its ability to generate

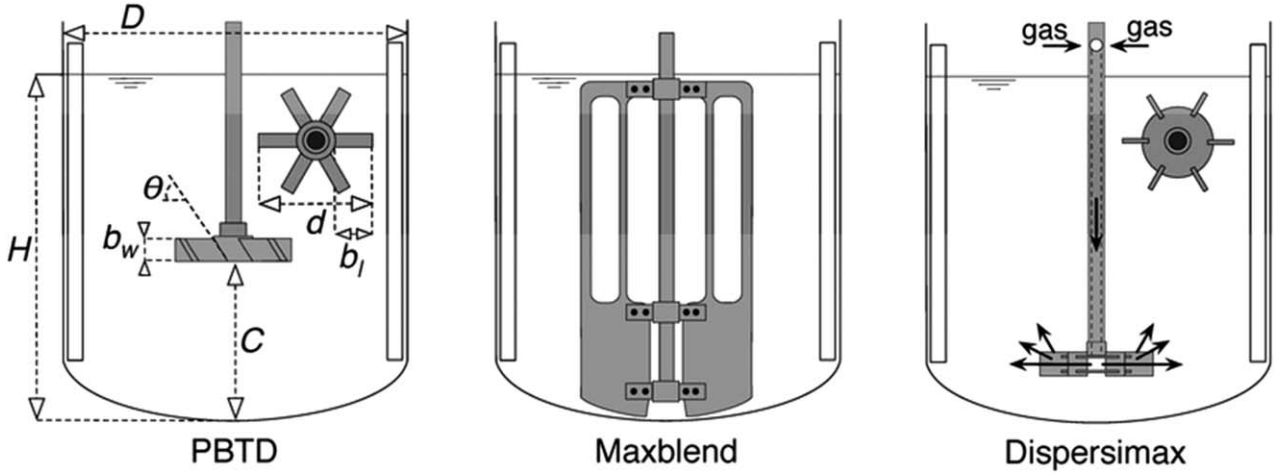

Figure 2. Schematics of the three impellers.

a very uniform shear field[45,47] and important gas entrainment in the liquid.[48] The Dispersimax is a gas-inducing-type impeller with a design similar to that of a classic disk turbine except that its blades are fixed on two slightly separated parallel disks instead of one. It mainly creates a radial flow and generates high shear levels.[42] Its main specificity is that it autonomously draws down the gas phase from the headspace of the vessel through a hollow shaft to the depression zones generated behind its blades where the gas is then dispersed as bubbles in the liquid phase. This type of impeller is well suited for gas-liquid contacting applications[42] and has been used by Linga et al.[30] and Happel et al.[40] to enhance the gas hydrate formation rate in setups similar to the one used in the present study. The dimensions and positions of the three impellers are standard and described in Table 1. The off-bottom clearance of the Dispersimax was deliberately chosen to be much smaller than the usual standard values as low off-bottom clearance values for disk turbine impellers have been shown to provide better solid dispersion capabilities.[49]

To characterize the power drawn by the three impellers during the hydrate formation experiments, a second mixing system is used. It consists of a transparent polycarbonate agitated vessel with the same dimensions and baffle arrangement as the vessel of the reactor used to perform the CO_2 hydrate formation experiments. The same impeller configurations as those used for the formation experiments are used. The impellers are driven by a variable speed DC motor. The power drawn by the impellers is determined by measuring the torque delivered by the motor using a torque transducer (model SS-050, 0–5 Nm, ± 0.2% span, Ono Sokki) placed between the motor and the agitator shaft. The torque measurement are performed using the same volume of distilled water as that used for the gas hydrate formation experiments, without adding any solids, at room temperature and atmospheric pressure. This second mixing system also allows visualizing the gas-liquid flow generated by the different impeller configurations (see "Aeration.mov," Supporting Information).

Table 1. Impeller Dimensions and Positions Parameters

		PBTD	Maxblend	Dispersimax
Tank diameter	D (m)	0.3	0.3	0.3
Liquid Height	H (m)	D	D	D
Impeller diameter	d (m)	$D/3$	$D/2$	$D/3$
Blade number	n	6	2	6
Blade angle	θ (°)	45	90	90
Blade length	b_l (m)	$d/3$	$d/2$	$d/4$
Blade width	b_w	$d/4$	$1.1D$	$d/5$
Off-bottom clearance	C (m)	$D/2$	$D/30$	$D/6$

Experimental procedure

CO_2 Hydrate Formation Experiments. Experiments in which only the flow conditions varied were performed to evaluate the impact of these flow conditions on the CO_2 hydrate formation rate, using a procedure similar to that classically employed to determine the kinetics of gas hydrate formation.[10,50] The procedure imposes a stepped pressure increment in a stirred tank in which a hydrate-forming gas is placed in contact in a semi-batch mode with a constant volume of liquid water, at a constant temperature. This liquid is initially (before the pressure increment) saturated with the gas and free of gas hydrate. The number of gas moles supplied to the tank over time to maintain the imposed pressure constant is measured. This number of moles of gas is hereafter referred to as the number of moles of gas consumed in the tank. The imposed pressure and the temperature used in this procedure are such that CO_2 hydrate formation is thermodynamically favorable. As presented hereafter, two stages can be easily seen in the obtained curve presenting the change over time of the total number of moles of gas consumed in the tank. One corresponds to CO_2 dissolution in the liquid without hydrate formation and the other corresponds to CO_2 hydrate particle growth in the liquid.

Each experiment begins by filling the reactor with 20 L of distilled water. The agitation and the thermostated circulating bath are then started. The temperatures in the jacket and reactor are allowed to stabilize at the operating temperature. The operating temperature is defined as the temperature at which, during an experiment, the temperature of the heat transfer fluid at the inlet of the jacket is controlled. The agitation is then stopped, the MFC bypass-valve is opened, and the reactor is rapidly pressurized to the operating pressure. The MFC bypass-valve is then closed, a 0.15 MPa overpressure is imposed between the inlet and outlet of the MFC and the pressure control is started. The agitation is then restarted at the experimental rotational speed. This last step defines the time zero of the measurement of the number of moles of gas consumed in the tank over time. The experiment is stopped 3 to 5 h

Table 2. Experimental Rotational Speeds of the Impellers and Corresponding ε_m

	Rotational Speed (rpm)	ε_m (W/kg)
PBTD	400	0.33
	500	0.52
	600	0.87
Maxblend	75	0.07
	100	0.15
	150	0.36
Dispersimax	400	0.52
	500	0.96
	650	2.19

after the hydrate particle growth stage has begun. The same operating pressure and temperature (2.5 MPa and 2°C) were used for all the experiments. The temperature increase of the heat transfer fluid between the inlet and outlet of the jacket of the tank never exceeded 0.75°C. Experiments were performed for each of the three impellers using a different set of three rotational speeds for each. Each experiment was repeated in duplicate, for a total of 18 CO_2 hydrate formation experiments.

The results of such a CO_2 hydrate formation experiment, obtained with a given impeller rotating at a given speed, are reported as functions of the power consumption per unit mass of liquid that would have been needed to rotate this impeller at this speed in the absence of gas hydrate particles, ε_m (W/kg). This quantity provides a relevant way to compare the relative performance of the impellers. The procedure used to determine ε_m is described in the previous section. The experimental rotational speeds of the impellers and the corresponding ε_m are given in Table 2.

Determination of the Volumetric Gas-Liquid Mass Transfer Coefficient and the Overall Heat Transfer Coefficient. In parallel with the hydrate formation experiments, gas dissolution and cooling experiments were performed with each of the flow conditions used for the hydrate formation experiments.

Gas dissolution experiments were performed to determine the volumetric gas-liquid mass transfer coefficient k_la (1/s), where k_l (m/s) is the gas-liquid mass transfer coefficient and a (m^2 of g-l interface/m^3 of liquid phase) is the volumetric gas-liquid interfacial area, corresponding to the flow conditions being studied. The procedure used for these experiments was similar to that used for the hydrate formation experiments. The same operating temperature was used, but the pressures used were below the hydrate formation pressure corresponding to this temperature. For a given dissolution experiment, knowing the number of moles of CO_2 consumed in the tank over time and knowing the solubility of CO_2 at the initial and imposed pressures,[51] the k_la can be determined.[52] At least three gas dissolution experiments were performed for each flow condition. The maximum relative standard error of these k_la measurements was 21.3%.

Cooling experiments were performed to determine the overall heat transfer coefficient between the bulk of the liquid in the reactor and the heat transfer fluid in the jacket, U (W/K m^2 of heat transfer surface), corresponding to the flow conditions being studied. The procedure used for these experiments consists of measuring the temperature of the bulk of the liquid in the reactor and of the heat transfer fluid at the inlet and outlet of the tank jacket over time after that a stepped decrease in temperature has been imposed to the set point of the thermostated circulating bath. During these experiments, the heat transfer fluid reaches the new set point temperature before the bulk of the liquid. U can be determined from the following equation, which is derived from an energy balance performed around the reactor after that the heat transfer fluid has reached the new set point temperature[53]

$$\ln\left(\frac{T_{SP}-T_0}{T_{SP}-T_{bulk}}\right)=\frac{SU}{V\rho_l c_p}t \tag{1}$$

where T_{SP}, T_0, and T_{bulk} are, respectively, the new set-point temperature, the temperature of the bulk of the liquid at the time at which the heat transfer fluid reaches T_{SP} and the temperature of the bulk of the liquid at time t (s). S (m^2) is the inner surface area of the wall of the tank in contact with the liquid, V (m^3) is the volume of the liquid, and ρ_l (kg/m^3) and c_p (kJ/kg K) are, respectively, the density and specific heat capacity of liquid water. At least two cooling experiments were performed for each flow condition. The maximum relative standard error of these U measurements was 5.4%.

Mathematical Model and Rate-Limiting Step Determination

Mathematical model

The system considered for the mathematical model of our experiments consists of growing CO_2 hydrate particles dispersed in an agitated continuous pure liquid phase in contact with a pure CO_2 gas phase. The system is kept at a constant pressure, its environment is kept at a constant temperature, and a quasi-steady state is assumed.

In order to characterize such a system, following the approach adopted by, for example, Mori[29] and Hashemi et al.,[54] an isobaric CO_2-in-water solubility diagram can be used. The diagram is composed of two equilibrium curves, $C^*_{g-l}(T)$ and $C^*_{l-H}(T)$ (mol/m^3 of liquid phase). $C^*_{g-l}(T)$ is the CO_2 concentration in liquid water at temperature T (°C) when the equilibrium between this liquid and a CO_2 gas phase at a given constant pressure is reached. $C^*_{l-H}(T)$ is the CO_2 concentration in liquid water at temperature T when the equilibrium between this liquid and a CO_2 hydrate solid phase is reached, at a given constant pressure. Figure 3 shows the

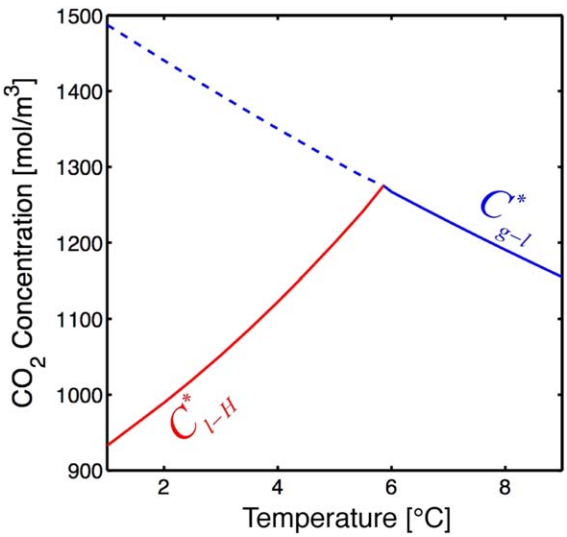

Figure 3. CO_2-in-water solubility diagram at 2.5 MPa, from Diamond and Akinfiev.[51]

[Color figure can be viewed in the online issue, which is available at wileyonlinelibrary.com.]

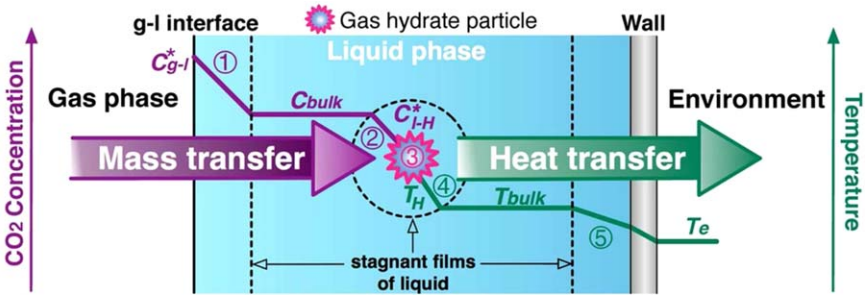

Figure 4. Schematic drawing of the model of the CO_2 hydrate formation process illustrating the driving forces (concentration and temperature gradients) of its five constitutive steps.

These steps are: ① the diffusion of the CO_2 molecules from the gas phase to the bulk of the liquid phase; ② the diffusion of the CO_2 molecules from the bulk of the liquid phase to the hydrate particle surface; ③ the integration of the CO_2 and H_2O molecules in the crystal lattice of the hydrate particle; ④ the heat transfer from the hydrate particle surface to the bulk of the liquid phase; ⑤ the heat transfer from the bulk of the liquid phase to the environment. [Color figure can be viewed in the online issue, which is available at wileyonlinelibrary.com.]

CO_2-in-water solubility diagram at the operating pressure used during the hydrate formation experiments, that is, 2.5 MPa. The dashed part of $C^*_{g-l}(T)$ represents a metastable equilibrium that characterizes the solubility of CO_2 in liquid water in the metastable absence of CO_2 hydrate. The intersection of the two equilibrium curves corresponds to the gas-liquid-hydrate three-phase equilibrium.

The mechanism leading to the incorporation of CO_2 molecules into the hydrate particle lattice involves a combination of mass and heat transfers, and can be decomposed into five steps that take place consecutively, as illustrated in Figure 4. These steps are presented below.

The growth of CO_2 hydrate particles requires water and CO_2 molecules. In our system, the hydrates are growing in the liquid phase, making the water molecules readily available, whereas the CO_2 molecules, which are initially present in the gas phase, have first to dissolve in the liquid. The first step of our model is thus the mass transfer of CO_2 molecules from the gas phase to the bulk of the liquid phase, which feeds the liquid phase with CO_2 molecules and sustains the growth of the hydrate particles. Based on the two-film theory, the CO_2 molecules diffuse through a thin stagnant film of fluid lying on each side of the gas-liquid interface. The diffusion is driven by a concentration gradient established across the films. Assuming a negligible resistance to mass transfer in the gas phase and an equilibrium between the gas phase and the liquid phase at their interface, the volumetric rate at which the gas is dissolved into the liquid phase, $\tilde{j}$ (mol/s m^3 of liquid phase), is given by the following equation

$$\tilde{j}=k_l a\left(C^*_{g-l}(T_{bulk})-C_{bulk}\right) \tag{2}$$

where T_{bulk} (°C) is the temperature of the bulk of the liquid phase and C_{bulk} (mol/m^3 of liquid phase) is the CO_2 concentration in the bulk of the liquid phase. Here, it is assumed that CO_2 consumption in the liquid phase due to the growth of the hydrate does not influence the rate of CO_2 dissolution, which is thus viewed as a simple physical gas absorption phenomenon.

Away from the thin films, the CO_2 concentration in the bulk of the liquid phase is assumed to be uniform due to sufficient agitation.

Hydrate growth in the liquid phase is generally represented by the diffusion-reaction theory, which is traditionally used to model crystal growth in solution crystallization.[10,55] Based on this theory, crystal growth proceeds in two consecutive steps. First, the dissolved CO_2 molecules diffuse from the bulk of the liquid phase to a liquid-solid interface through a thin stagnant film of liquid adjacent to the interface. The diffusion is driven by a concentration gradient established across the liquid film. These molecules, together with water molecules, then integrate the crystal lattice of the hydrate particle. The integration is also believed to be driven by an ambiguous concentration gradient established across a mono-molecular-thick adsorption layer sitting on the hydrate surface. These mass transfer and integration phenomena are, respectively, the second and the third steps of our model. Assuming that there is no accumulation of CO_2 molecules in the stagnant film of liquid adjacent to a particle surface, the rate at which the CO_2 molecules are transferred through such liquid films and incorporated into the particles are equal. If it is further assumed that the thicknesses of the liquid films are small compared with the particles size, the CO_2 hydrate formation rate, j (mol/s m^3 of liquid phase), is given by the following equation

$$j=4\pi\mu_2 k_s K_g\left(C_{bulk}-C^*_{l-H}(T_H)\right) \tag{3}$$

where μ_2 (m^2 of hydrate particle surface/m^3 of liquid phase) is the second-order moment of the hydrate particle size distribution given by

$$\mu_2=\int_0^\infty L^2 n(L)dL \tag{4}$$

L (m) and $n(L)$ (number of hydrate particles/m m^3 of liquid phase) are a characteristic size of the hydrate particles and the number density function, respectively. k_s is the surface shape factor of the hydrate particles ($k_s = 1$ for spherical particles if L is the radius of the particles). $4\pi\mu_2 k_s$ is the surface area of the hydrate particles per unit of volume of the liquid phase. K_g (m/s) is the hydrate global growth coefficient that can be written as follows

$$\frac{1}{K_g}=\frac{1}{k_d}+\frac{1}{k_i} \tag{5}$$

where k_d (m/s) and k_i (m/s) are the mass transfer coefficient in the stagnant film of liquid surrounding a hydrate particle and the kinetic constant of the integration of the dissolved CO_2 and water molecules in the lattice of these particles, respectively. T_H (°C) is the temperature of the hydrate particle surface.

Gas hydrate formation is an exothermic phenomenon. The heat released has to be continuously removed to the

environment. Heat is initially released at a growing hydrate particle surface where it generates a temperature increase relatively to the temperature of the bulk of the liquid phase. The heat is then transferred to the bulk of the liquid phase and is finally transferred from the bulk of the liquid phase to the environment. Heat transfer from a hydrate particle surface to the bulk of the liquid phase takes place through a thin stagnant film of liquid adjacent to the particle and is driven by the temperature gradient established across the film. This heat transfer phenomenon is the fourth step of our model. The following energy balance performed around the hydrate particles links the heat transfer rate from the particle surfaces to the bulk of the liquid phase with j

$$\mathcal{L}j = 4\pi\mu_2 k_s h (T_H - T_{bulk}) \tag{6}$$

where $\mathcal{L}$ (J/mol) is the latent heat of CO_2 hydrate formation and h (W/K m^2 of hydrate surface) is the heat transfer coefficient between a hydrate particle and the bulk of the liquid phase.

Away from the thin films, the temperature of the bulk of the liquid phase is assumed to be uniform due to sufficient agitation.

Heat transfer from the bulk of the liquid phase to the environment is the fifth and last step of our model. The following energy balance performed around the whole system links the heat transfer rate from the bulk of the liquid phase to the environment with j

$$\mathcal{L}j = \frac{SU}{V}(T_{bulk} - T_e) \tag{7}$$

where S (m^2) is the surface area of the wall of the system in contact with the liquid phase, V (m^3) is the volume of the liquid phase, U (W/K m^2 of heat transfer surface) is the overall heat transfer coefficient between the bulk of the liquid and the system environment, and T_e (°C) is the temperature of the environment.

It can be observed that the driving forces of the three first steps of our model are appearing in Eqs. 2 and 3 in the form of concentration gradients, while the ones of the two last steps are appearing in Eqs. 6 and 7 in the form of temperature gradients. To be able to combine these equations, the two following equations, respectively resulting from the linearization of $C^*_{l-H}(T)$ around T_e for $T = T_{bulk}$ and $T = T_H$, are used to rewrite the temperature gradients appearing in Eqs. 6 and 7 in terms of concentration gradients

$$C^*_{l-H}(T_{bulk}) = C^*_{l-H}(T_e) + \frac{dC^*_{l-H}}{dT}\Big|_{T_e}(T_{bulk} - T_e) \tag{8}$$

and

$$C^*_{l-H}(T_H) = C^*_{l-H}(T_e) + \frac{dC^*_{l-H}}{dT}\Big|_{T_e}(T_H - T_e) \tag{9}$$

Using these two equations, Eqs. 6 and 7 can be, respectively, rewritten as follows:

$$j = \frac{4\pi\mu_2 k_s h}{\mathcal{L}}\left(\frac{dC^*_{l-H}}{dT}\Big|_{T_e}\right)^{-1}\left(C^*_{l-H}(T_H) - C^*_{l-H}(T_{bulk})\right) \tag{10}$$

and

$$j = \frac{SU}{\mathcal{L}V}\left(\frac{dC^*_{l-H}}{dT}\Big|_{T_e}\right)^{-1}\left(C^*_{l-H}(T_{bulk}) - C^*_{l-H}(T_e)\right) \tag{11}$$

Owing to the quasi-steady state assumption, it is assumed that $\tilde{j} = j$. Therefore, by combining Eqs. 2, 3, 10, and 11, it follows that

$$j = \frac{C^*_{g-l}(T_{bulk}) - C^*_{l-H}(T_e)}{\frac{1}{k_l a} + \frac{1}{4\pi\mu_2 k_s K_g} + \frac{\mathcal{L}}{4\pi\mu_2 k_s h}\frac{dC^*_{l-H}}{dT}\Big|_{T_e} + \frac{\mathcal{L}V}{SU}\frac{dC^*_{l-H}}{dT}\Big|_{T_e}} \tag{12}$$

The numerator $C^*_{g-l}(T_{bulk}) - C^*_{l-H}(T_e)$ is the global driving force of CO_2 hydrate formation. It is equal to the sum of the individual driving forces associated with each of the constitutive steps of hydrate formation described above. The denominator is the global resistance to CO_2 hydrate formation, R_{global} (s). It is composed of four terms

$$R_1 = \frac{1}{k_l a}(\text{s}) \tag{13}$$

$$R_{2-3} = \frac{1}{4\pi\mu_2 k_s K_g}(\text{s}) \tag{14}$$

$$R_4 = \frac{\mathcal{L}}{4\pi\mu_2 k_s h}\frac{dC^*_{l-H}}{dT}\Big|_{T_e}(\text{s}) \tag{15}$$

$$R_5 = \frac{\mathcal{L}V}{SU}\frac{dC^*_{l-H}}{dT}\Big|_{T_e}(\text{s}) \tag{16}$$

If $R_1 \gg R_{2-3}$, R_4, and R_5, Eq. 12 simplifies into

$$j \approx \left(C^*_{g-l}(T_{bulk}) - C^*_{l-H}(T_e)\right)/R_1 \tag{17}$$

If Eq. 17 is then compared with Eq. 2, it can be seen that $R_1 \gg R_{2-3}$, R_4, and R_5 implies $C_{bulk} \approx C^*_{l-H}(T_e)$. As $C^*_{l-H}(T)$ is an increasing function of T (see Figure 3), as $T_H > T_{bulk} > T_e$, and as C_{bulk} is necessarily larger than $C^*_{l-H}(T_H)$ for hydrate particles to grow, $C_{bulk} \approx C^*_{l-H}(T_e)$ leads to $T_H \approx T_{bulk} \approx T_e$. Therefore, $R_1 \gg R_{2-3}$, R_4, and R_5 means that the steps 2, 3, 4, and 5 of our model of the hydrate formation process are almost at equilibrium. Gas dissolution in the liquid is thus the rate-limiting step of the CO_2 hydrate formation process, and R_1 can be seen as the resistance of this step.

If $R_5 \gg R_1$, R_{2-3}, and R_4, Eq. 12 simplifies into

$$j \approx \left(C^*_{g-l}(T_{bulk}) - C^*_{l-H}(T_e)\right)/R_5 \tag{18}$$

If Eq. 18 is compared with Eq. 11, it can be seen that $R_5 \gg R_1$, R_{2-3}, and R_4 implies $C^*_{l-H}(T_{bulk}) \approx C^*_{g-l}(T_{bulk})$. Therefore, T_{bulk} is close to the temperature at which the two equilibrium curves $C^*_{g-l}(T)$ and $C^*_{l-H}(T)$ intersect (see Figure 3). As $C^*_{l-H}(T)$ is an increasing function of T, as $T_H > T_{bulk}$, and as C_{bulk} is necessarily larger than $C^*_{l-H}(T_H)$ and lower than $C^*_{g-l}(T_{bulk})$ for hydrate particles to grow, $C^*_{l-H}(T_{bulk}) \approx C^*_{g-l}(T_{bulk})$ leads to $T_H \approx T_{bulk}$ and to $C_{bulk} \approx C^*_{l-H}(T_{bulk}) \approx C^*_{g-l}(T_{bulk})$. Therefore, $R_5 \gg R_1$, R_{2-3}, and R_4 means that the steps 1, 2, 3, and 4 of our model of the hydrate formation process are almost at equilibrium. Heat transfer to the environment is the rate-limiting step of the CO_2 hydrate formation process, and R_5 can be seen as the resistance of this step.

If $R_{2-3} \gg R_1$, R_4, and R_5, Eq. 12 simplifies into

$$j \approx \left(C^*_{g-l}(T_{bulk}) - C^*_{l-H}(T_e)\right)/R_{2-3} \tag{19}$$

By combining Eqs. 3, 10, and 11, and if $R_{2-3} \gg R_1$, R_4, and R_5, it can then be written that

$$\begin{aligned} j &= \left(C_{bulk} - C^*_{l-H}(T_e)\right)/(R_{2-3} + R_4 + R_5) \\ &\approx \left(C_{bulk} - C^*_{l-H}(T_e)\right)/R_{2-3} \end{aligned} \tag{20}$$

By comparing the last two equations and Eq. 3, it is observed that $R_{2-3} \gg R_1$, R_4, and R_5 implies $T_H \approx T_e$ (and

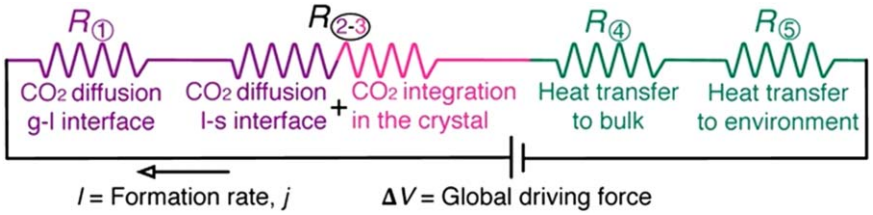

Figure 5. Electrical circuit analogy of the CO_2 hydrate formation process.

[Color figure can be viewed in the online issue, which is available at wileyonlinelibrary.com.]

hence $T_{bulk} \approx T_e$) and $C_{bulk} \approx C^*_{g-l}(T_{bulk})$. This means that the steps 1, 4, and 5 of our model of the hydrate formation process are almost at equilibrium. Hydrate growth in the liquid phase is the rate-limiting step of the CO_2 hydrate formation process, and R_{2-3} can be seen as the resistance of this step.

R_4 can be seen as the resistance associated with heat transfer from hydrate surfaces to the bulk of the liquid phase. To gain greater insight on the respective importance of R_{2-3} and R_4 in $R_{2-3}+R_4$, it is instructive to evaluate the order of magnitude of the ratio between these two resistances. As $K_g < k_d$ (see Eq. 5), it can be written that

$$\frac{R_4}{R_{2-3}} < \frac{\mathcal{L}k_d}{h}\frac{dC^*_{l-H}}{dT}\bigg|_{T_e} \tag{21}$$

Using traditional correlations to calculate the Nusselt and Sherwood numbers for a sphere in a flow,[56] it can be written that

$$\frac{k_d}{h} \approx \frac{\mathbb{D}}{\lambda}\left(\frac{\lambda}{\rho c_p \mathbb{D}}\right)^{1/3} \tag{22}$$

where λ (W/m K), ρ (kg/m^3), and c_p (kJ/kg K) are the thermal conductivity, the density, and the specific heat capacity of liquid water, respectively. $\mathbb{D}$ (m^2/s) is the diffusion coefficient of CO_2 in liquid water. λ, ρ, c_p, and $\mathbb{D}$ are approximately equal to 0.6 W/m K, 1000 kg/m^3, 4 kJ/kg K, and 1×10^{-9} m^2/s, respectively. R_4/R_{2-3} is thus $< \sim 10^{-2}$. Therefore, $R_{2-3} + R_4 \approx R_{2-3}$, that is, the transfer of heat from the surface of the hydrate particles toward the bulk of the liquid phase has a negligible influence on the CO_2 hydrate growth kinetics in the liquid. This also implies that the temperature increase at the hydrate surface is small and therefore that $T_H \approx T_{bulk}$. Using a reasoning based on Eq. 6 and experimental values for j and μ_2 measured for CO_2 hydrate formation in a semi-batch stirred tank reactor, Hashemi et al.[54] arrived at a similar conclusion. The value of the right hand side of Eq. 21 have been defined by Matsuoka and Garside[57] as a measure of the contribution to crystal growth of heat transfer from the crystals to the bulk of the liquid phase. They empirically found that the effect of heat transfer on the kinetics of crystal growth can be ignored when this value is smaller than 10^{-2}; this supports our analysis.

As seen in the previous paragraphs, R_{global} is the sum of the individual resistances that can be assigned to each steps of the CO_2 hydrate formation process. An electrical circuit analogy of this process, presented in Figure 5, can therefore be proposed. It consists of four resistances in series trough which a current, I, assimilated to j, is circulated thanks to a potential difference, ΔV, assimilated to the global driving force of the hydrate formation process. Applying Ohm's law to this circuit gives Eq. 12.

Equation 12 relies on the linearization of $C^*_{l-H}(T)$ around T_e (see Eqs. 8 and 9). The values of T_{bulk} and T_H during the CO_2 hydrate formation experiments performed in this work are always between $T_e \approx 2$°C, that is, the temperature of the heat transfer fluid flowing in the jacket of the reactor, and the temperature of the gas-liquid-hydrate three-phase equilibrium, which is approximately equal to 5.9°C at the operating pressure used (see Figure 3). Consequently, it can be shown that the values of $C^*_{l-H}(T_{bulk})$ and $C^*_{l-H}(T_H)$ calculated with Eqs. 8 and 9 differ at most by only 4% from their actual values (given in Figure 3). As such, this linearization provides a good estimation of these concentrations.

Rate-limiting step determination

To identify the rate-limiting step of the CO_2 hydrate formation process during a given experiment, two methods are proposed.

The first method uses the mathematical model built in the previous section and is based on the evaluation and comparison of the different individual resistances making up R_{global}.

For a given CO_2 hydrate formation experiment, R_1 and R_5 are determined from dissolution and cooling experiments, respectively. These experiments, described in the experimental procedure section, are performed in parallel with the hydrate formation experiment using the same impeller and the same rotational speed. They do not involve solids and are performed under temperature and pressure conditions that do not allow hydrate formation. It is assumed here that for low solid fractions the actual k_la and U values during a given hydrate formation experiment are constant and are equal to their respective values determined from these dissolution and cooling experiments, that is, k_la and U are not affected by the presence of growing hydrate particles in the liquid phase. V and S in the expression of R_5 (see Eq. 16) are known constant experimental parameters that are equal to 0.02 m^3 and 0.36 m^2, respectively. For our experimental setup, the environment to which the tank is subjected is the heat transfer fluid flowing in the jacket, and T_e is therefore the temperature of this fluid during the hydrate formation experiments, that is, $T_e \approx 2$°C. With the experimental conditions used in this work, the terms $dC^*_{l-H}/dT|_{T_e}$ and $\mathcal{L}$ are approximately equal to 59.8 mol/K m^3 of liquid phase (from the C^*_{l-H} curve of Figure 3) and 70.8 kJ/mol (CO_2 hydrate dissociation enthalpy at 5.5°C and 2.55 MPa[58]), respectively.

For a given CO_2 hydrate formation experiment, R_{2-3} is evaluated from Eq. 12, after determining the values of all the other terms in this equation. j and T_{bulk} are measured. Note that j is simply the time derivative of the number of moles of gas consumed in the tank during the hydrate particle growth stage divided by the volume of liquid in the tank. R_1 and R_5 are evaluated as explained above. $C^*_{g-l}(T_{bulk})$ and $C^*_{l-H}(T_e)$ are thermodynamic data obtained from Figure 3.

The second method used to identify the rate-limiting step of the CO_2 hydrate formation process is based on the identification, during the hydrate particle growth stage of an experiment, of the representative point of the system in the phase

diagram presented in Figure 3. This representative point has, by definition, T_{bulk} as the abscissa and C_{bulk} as the ordinate. To identify the rate-limiting step, this representative point can be compared with the points that would have been obtained if the hydrate formation process was solely limited by one of the constitutive steps of hydrate formation. For a given CO_2 hydrate formation experiment, T_{bulk} is measured directly. C_{bulk} is evaluated during the hydrate particle growth stage using Eq. 2, after determining the values of all the other terms in this equation. j is measured directly. k_la is evaluated as explained previously. $C^*_{g-l}(T_{bulk})$ is a thermodynamic data obtained from Figure 3.

Effect of an increase of the mixing intensity on the rate-limiting step

It can be expected that each of the identified resistances decreases when the mixing intensity increases. Indeed, all these resistances involve a heat or mass transfer coefficient in their denominator, and numerous studies have shown that these coefficients are increasing functions of the mixing intensity.[42,55,59,60] At sufficiently high mixing intensity, R_1 and R_4 should eventually become smaller than R_{2-3} and R_5. Indeed, R_1 and R_4 should tend to zero for a mixing intensity tending to the infinity. On the other hand, R_{2-3} and R_5 have non-zero theoretical minimal values, corresponding to a crystal growth limited by the integration of the dissolved CO_2 and water molecules in the lattice of the hydrates,[61] and to a heat exchange with the environment controlled by conduction across the walls of the system[42], respectively. Hence, regarding the intensification of a HBCS process by an optimization of the flow conditions, the three following questions should be addressed:

- Does the available equipment allow providing the mixing intensity necessary to decrease R_1 and R_4 to sufficiently low values such that the gas hydrate formation rate would be either limited by R_{2-3} or R_5, at their minimal values?
- If yes, which resistance, between R_{2-3} and R_5, would actually limit the formation rate? The answer to the latter question is of prime importance for the definition of scale up strategy if the questions are answered for a pilot equipment such as the one used in this work.
- Among the different configurations (choice of impeller, rotational speed, ...) of the selected equipment leading to a gas hydrate formation rate either limited by R_{2-3} or R_5, which one has the best energy performance?

Results and Discussion

Typical results: Consumption and temperature curves

Figure 6 shows the change over time of the total number of moles of gas consumed in the tank and of T_{bulk} obtained from a CO_2 hydrate formation experiment performed with the Dispersimax rotating at 500 rpm ($\varepsilon_m = 0.96$ W/kg). The shapes of the two curves are typical of all the experiments performed. The curve of the change over time of the total number of moles of gas consumed in the tank is hereafter referred to as the consumption curve.

The first part of the consumption curve corresponds to the dissolution of CO_2 in the liquid following the stepped pressure increment imposed at time zero. During the dissolution process, the concentration of CO_2 in the liquid increases progressively and reaches $C^*_{l-H}(T_{bulk})$. From this point, the supersaturation regarding CO_2 hydrate builds up and CO_2 hydrate formation may occur in the liquid. However, the concentration of CO_2 in the liquid typically reaches $C^*_{g-l}(T_{bulk})$

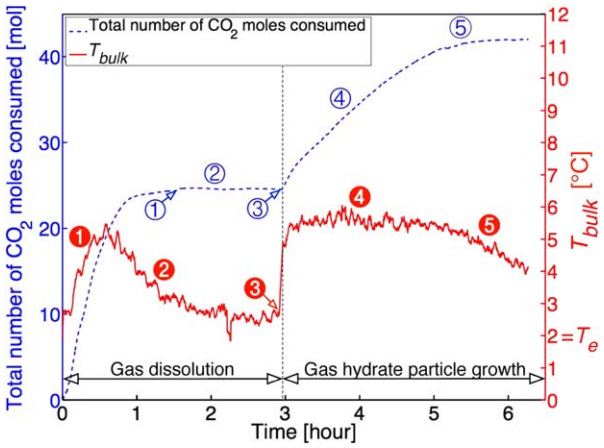

Figure 6. Change over time of T_{bulk} and of the total number of moles of gas consumed in the tank, obtained from a CO_2 hydrate formation experiment performed with the Dispersimax rotating at 500 rpm ($\varepsilon_m = 0.96$ W/kg).

[Color figure can be viewed in the online issue, which is available at wileyonlinelibrary.com.]

before any indication of the beginning of CO_2 hydrate formation could have been observed. Once this concentration has been reached, the gas consumption rate falls to zero (① on the consumption curve). The system can then stay in this metastable state for a significant length of time (② on the consumption curve), typically 1–2 h, before CO_2 hydrate formation manifests itself macroscopically by a sudden increase in the gas consumption rate (③ on the consumption curve). This sudden increase marks the beginning of the second part of the consumption curve, which corresponds to the growth of the CO_2 hydrate particles. The CO_2 hydrate formation rate, j, given by the slope of this part of the consumption curve divided by the volume of liquid in the tank, rapidly reaches and stays at an almost constant value (④ on the consumption curve), depending of the experimental conditions, for a few hours before slowly decreasing to zero (⑤ on the consumption curve).

At the beginning of an experiment, T_{bulk} first increases rapidly (❶ on the T_{bulk} curve) due to the release of the enthalpy of dissolution associated with the gas absorption process and then gradually drops back to T_e (❷ on the T_{bulk} curve) as the gas absorption slows down. At the onset of CO_2 hydrate formation, T_{bulk} rises abruptly by a few degrees (❸ on the T_{bulk} curve) due to the release of the enthalpy of formation of a large amount of gas hydrates. This abrupt rise of T_{bulk} is the second macroscopic indication of the beginning of the CO_2 hydrate formation process. The curve showing the change over time of T_{bulk} then exhibits a plateau (❹ on the T_{bulk} curve), or a very low negative slope comparable to a plateau, at a value depending of the experimental conditions. T_{bulk} stays at this value as long as the formation rate stays almost constant and then progressively decreases to T_e (❺ on the T_{bulk} curve) as soon as the formation rate decreases.

The discussion of the experimental results, presented below, focuses on the period of almost constant hydrate formation rate (④ on the consumption curve) that follows the onset of gas hydrate particle growth.

CO_2 hydrate formation rate vs. flow conditions

Figure 7 shows the CO_2 hydrate formation rate, j, measured during the almost constant formation rate period that follows the onset of the gas hydrate particle growth, as a function of

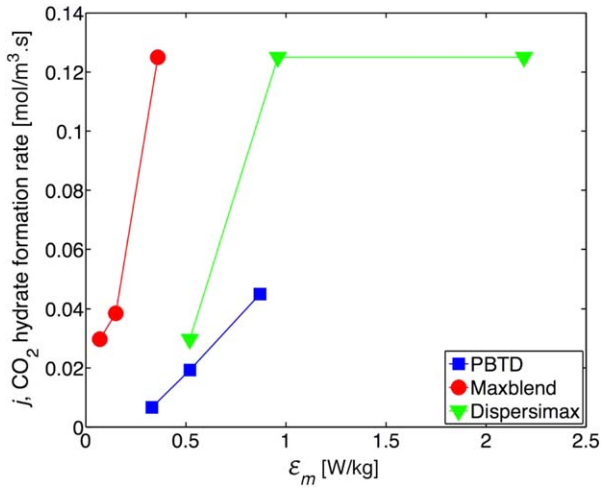

Figure 7. CO_2 hydrate formation rate, *j*, measured after the onset of gas hydrate particle growth, as a function of ε_m for the three impellers studied.

[Color figure can be viewed in the online issue, which is available at wileyonlinelibrary.com.]

ε_m for the three impellers studied. Each point represents the average of two replicates. The maximum relative standard error of these *j* measurements is 21.7%. It can be seen that *j* increases with ε_m for all three impellers. For the Dispersimax, it appears that at $\varepsilon_m > 0.5$ W/kg a *j* maximum approximately equal to 0.125 mol/s m^3 is reached. It has to be noted that the *j* measured for the Maxblend at the highest ε_m has almost the same value than the *j* maximum measured for the Dispersimax. This *j* value is not reached by the PBTD. It can also be seen that the PBTD and the Dispersimax present similar *j* values at $\varepsilon_m \approx 0.5$ W/kg. However, at $\varepsilon_m \approx 0.9$ W/kg, the Dispersimax has a *j* value significantly larger than the one of the PBTD. Last, the figure also shows that the Maxblend has the largest j/ε_m ratio by far.

Resistances of the constitutive steps of the CO_2 hydrate formation process vs. flow conditions

Figures 8a, b, and c show R_1, R_{2-3}, and R_5, during the almost constant formation rate period, calculated using the method described in the rate-limiting step determination section, as functions of ε_m for the PBTD, Maxblend, and Dispersimax, respectively. These figures show that R_1 and R_{2-3} significantly decrease with an increase in ε_m, while R_5 appears to be almost independent of this quantity for the three impellers in their respective range of ε_m studied. This is consistent with the fact that *j* increases when ε_m increases for the three impellers, as shown in Figure 7.

Figures 9a, b, and c respectively show R_1, R_{2-3}, and R_5, during the almost constant formation rate period, as functions of ε_m for the three impellers used in this study.

Figure 9a shows that, as expected, R_1 decreases when ε_m increases, for the three impellers. For the Dispersimax and the Maxblend, a large relative decrease of R_1 is observed, when ε_m increases from its smallest to it largest value. The smallest values of R_1 obtained with the Dispersimax and the Maxblend are close to each other. While the range of ε_m at which the PBTD was used was similar than the ones used for the other two impellers, a limited relative decrease of R_1 is observed for the PBTD. Moreover, the minimal value of R_1 obtained for the PBTD is way larger than the ones obtained for the Maxblend and the Dispersimax. These observations can be explained with the help of the experiments, described in the experimental method section, performed using the polycarbonate vessel for the determination of ε_m, which also allowed visually assessing the gas-liquid contact generated by the different impeller configurations (see "Aeration.mov," Supporting Information). This visualization allows identifying two mechanisms responsible of this contact.

The first mechanism of gas-liquid contact, only active for the Dispersimax, is the pumping of the gas from the tank headspace to the reactor bottom, through the hollow shaft of the impeller, and its consecutive dispersion as bubbles in the liquid. As it can be seen in the movie "Aeration.mov" (Supporting Information), the large relative decrease of R_1 for the Dispersimax when ε_m increases from ~0.5 to ~0.9 W/kg can be attributed to the fact that the gas induction mechanism begins to be very intense at ε_m values > 0.5 W/kg.

The second mechanism of gas-liquid contact, active for all three impellers, is the gas entrainment from the tank headspace into the liquid due to the combined effect of deformation and breakage of the open surface of the liquid, bubble entrapment,

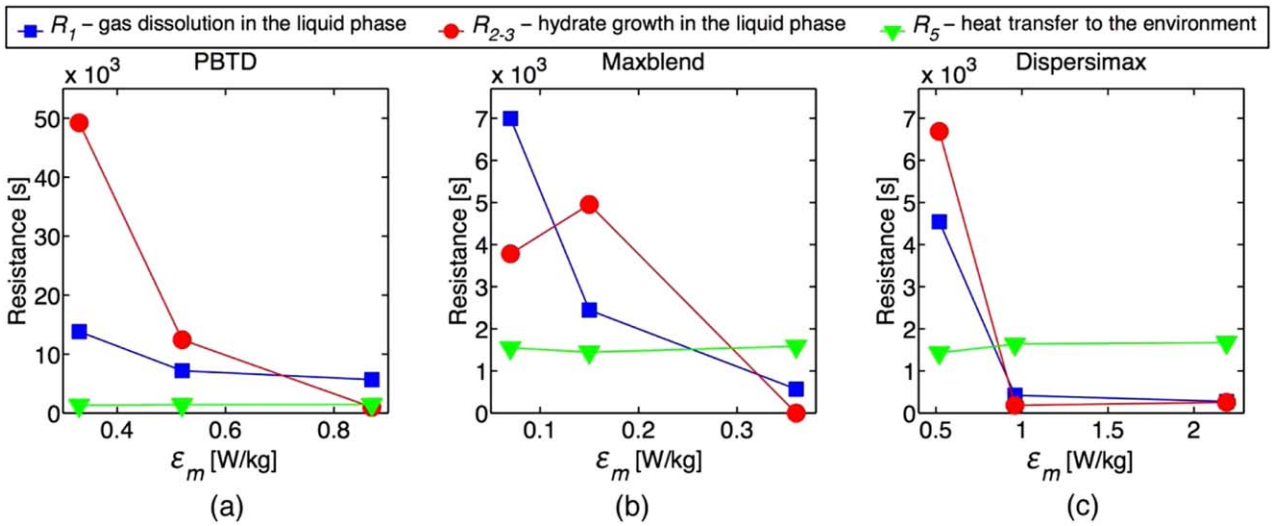

Figure 8. R_1, R_{2-3}, and R_5, during the almost constant formation rate period, as functions of ε_m for the PBTD (a), Maxblend (b), and Dispersimax (c).

[Color figure can be viewed in the online issue, which is available at wileyonlinelibrary.com.]

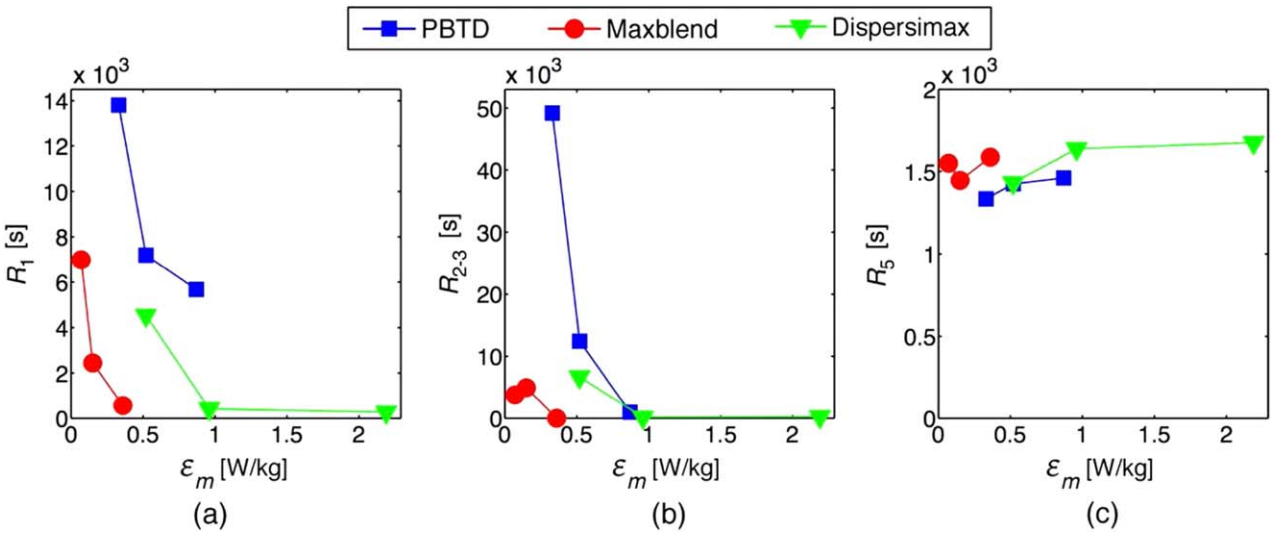

Figure 9. R_1 (a), R_{2-3} (b), and R_5 (c), during the almost constant formation rate period, as functions of ε_m for the three impellers used in this study.

[Color figure can be viewed in the online issue, which is available at wileyonlinelibrary.com.]

and liquid flow circulation underneath the open surface.[48,62] The capacity of the Maxblend to reduce R_1 nearly as much as the Dispersimax, even if it is not a gas-inducing type impeller, can be attributed to the fact that this second type of gas-liquid contact mechanism appears to be especially active for this impeller (see the "Aeration.mov"). The poor performance of the PBTD in reducing R_1 can be explained by its poor ability to provide high levels of gas entrainment in the liquid.

Figure 9b shows that, as expected, R_{2-3} decreases when ε_m increases, for the three impellers. Whatever the impeller, the relative decrease of R_{2-3} is important, when ε_m increases from its smallest to it largest value. The smallest values of R_{2-3} obtained with the three impellers are close to each other. This can reasonably be attributed to the fact that the demonstrated ability of these impellers to provide a good quality of solid suspension and high shear levels[42,46] is fully developed at the highest mixing intensities considered, while it is not fully developed at the smallest mixing intensities considered. It is interesting to note that the extent of the relative decrease (in percent) of R_{2-3} when ε_m increases from ~0.5 to ~0.9 W/kg is similar for the PBTD and the Dispersimax.

Figure 9c shows that R_5 is not only almost independent of ε_m for the three impellers, as already seen in Figures 8a, b, and c, but is also almost independent of the type of impeller used. Therefore, it can reasonably be assumed that, whatever the impeller and the mixing intensity used, the heat transfer to the environment is mainly limited by heat conduction through the relatively thick wall of the reactor (1 cm).

From the above discussion, the fact that j increases much more for the Dispersimax than for the PBTD when ε_m increases from ~0.5 to ~0.9 W/kg, as observed in Figure 7, can be reasonably attributed to the important intensification of the Dispersimax gas induction mechanism at ε_m values > 0.5 W/kg and the identified poor ability of the PBTD to provide high levels of liquid aeration.

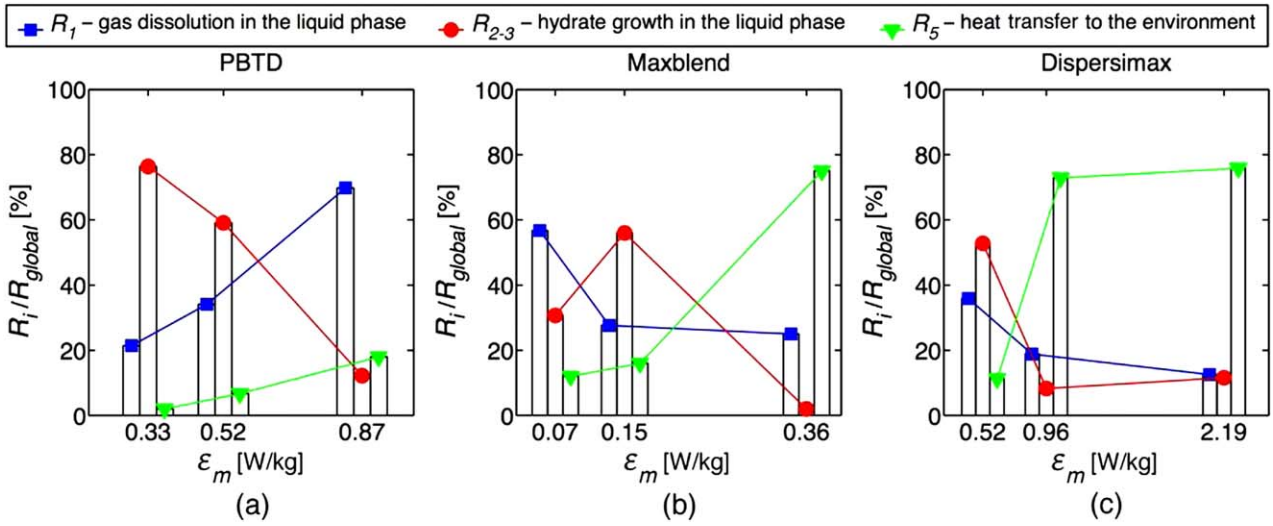

Figure 10. R_1/R_{global}, R_{2-3}/R_{global}, and R_5/R_{global} during the almost constant formation rate period, as functions of ε_m for the PBTD (a), Maxblend (b), and Dispersimax (c).

[Color figure can be viewed in the online issue, which is available at wileyonlinelibrary.com.]

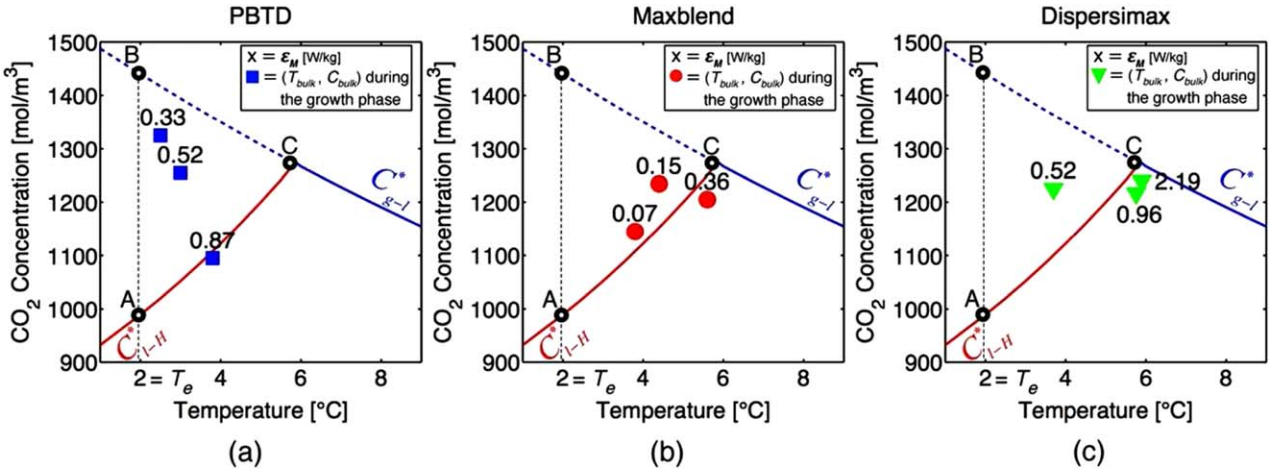

Figure 11. Representative points of the system in the CO_2-in-water solubility diagram at the experimental operating pressure (2.5 MPa), as a function of ε_m during the almost constant formation rate period for the PBTD (a), Maxblend (b), and Dispersimax (c).

[Color figure can be viewed in the online issue, which is available at wileyonlinelibrary.com.]

Determination of the rate-limiting step of the CO_2 hydrate formation process via the relative weight of the resistances of the constitutive steps of CO_2 hydrate formation

Figures 10a, b, and c show R_1/R_{global}, R_{2-3}/R_{global}, and R_5/R_{global} during the almost constant formation rate period, as functions of ε_m for the PBTD, Maxblend, and Dispersimax, respectively. These figures show that the rate-limiting step of the CO_2 hydrate formation rate, that is, the step exhibiting the largest resistance, changes with ε_m for all three impellers. They also show that, for given flow conditions, while there is always one step that can be considered as rate-limiting, the resistances of the other steps are not necessarily negligible. For the PBTD, as ε_m increases, the formation rate is first mainly limited by hydrate growth in the liquid phase and then by gas dissolution in the liquid phase. For the Maxblend, as ε_m increases, the formation rate is first mainly limited by gas dissolution in the liquid phase, then by hydrate growth in the liquid phase, and finally by heat transfer to the environment. For the Dispersimax, as ε_m increases, the formation rate is first mainly limited by hydrate growth in the liquid phase and then by heat transfer to the environment. It is interesting to note that, for the three impellers used in the present study, at low ε_m in their respective range of ε_m investigated, the formation rate is limited by a mass transfer step, either gas-liquid or liquid-solid. At higher ε_m, the rate-limiting step switches to the heat transfer to the environment step for the Maxblend and the Dispersimax. It is reasonable to assume that the same shift would have been observed for the PBTD if larger ε_m had been used. This shift can be explained by the fact, already mentioned above, that the resistances associated with the mass transfer steps decrease with ε_m while the resistance to the heat transfer to the environment step seems to be independent of this quantity. R_5/R_{global} thus increases as ε_m increases, up to a point where heat transfer to the environment limits the formation rate.

It is interesting to note that heat transfer limitations are observed at the relatively small scale used to perform our CO_2 hydrate formation experiments. This fact, which is not often reported in the literature, is an important finding for the development of scaling-up strategies for hydrate-based gas separation processes. It can be mainly attributed to the relatively high latent heat associated with gas hydrate formation, which has made them, in addition to gas separation applications, interesting candidates for refrigeration applications.[63]

From the facts that, at high ε_m, the resistance to heat transfer to the environment limits the CO_2 hydrate formation rate for both the Maxblend and the Dispersimax and that, as shown in the Figure 9c, this resistance is independent of the flow conditions, it may reasonably be inferred that the j value measured for the Dispersimax at $\varepsilon_m > 0.5$ W/kg and the j value measured for the Maxblend at the highest ε_m (see Figure 7) both correspond to the maximum value of j achievable under the conditions used during the formation experiments. This maximal value of j corresponds to the CO_2 hydrate formation rate allowed by the resistance to heat transfer to the environment when the other resistances have decreased to negligible levels due to sufficient mixing intensity.

Determination of the rate-limiting step of the CO_2 hydrate formation process via the representative point position in the CO_2-in-water solubility diagram

Figures 11a, b, and c show the effect of ε_m on the representative point of the system in the CO_2-in-water solubility diagram at the operating pressure during the almost constant formation rate period for the PBTD, Maxblend, and Dispersimax, respectively. The method used to identify these points is described in the rate-limiting step determination section. In Figures 11a, b, and c, points A, B, and C are the representative points that would have been obtained if the hydrate formation process was solely limited by one of the constitutive steps of hydrate formation. Point A corresponds to a process limited by gas dissolution in the liquid ($C_{bulk} = C^*_{l-H}(T_e)$ and $T_{bulk} = T_e$, that is, the other steps are at equilibrium). Point B corresponds to a process limited by hydrate growth in the liquid phase ($C_{bulk} = C^*_{g-l}(T_e)$ and $T_{bulk} = T_e$, that is, the other steps are at equilibrium). Point C corresponds to a process limited by heat transfer to the environment ($C_{bulk} = C^*_{l-H}(T_{bulk}) = C^*_{g-l}(T_{bulk})$, that is, the other steps are at equilibrium and the representative point corresponds to the three-phase equilibrium).

The representative points shown in these figures have positions that are consistent with the observations made with respect to Figures 10a, b, and c. For given flow conditions, the position of the representative point of the system appears to be mainly determined by the rate-limiting step but, at the same time, is influenced by the other steps with non-negligible resistances. For the PBTD, the progressive transition, as ε_m increases, from a hydrate formation rate mainly limited by hydrate growth in the liquid phase to a hydrate formation rate mainly limited by gas dissolution in the liquid phase is clearly represented by the migration of the position of the representative points of the system from a position close to point "B" to a position close to point "A." The slight temperature drift of the position of the representative points of the system towards point "C" as ε_m increases is a manifestation of the growing weight of the resistance to heat transfer to the environment. For the Maxblend, the positions of the representative points of the system for the lowest and the intermediate ε_m, close to points "A" and "B," respectively, depict a transition, as ε_m increases, from a hydrate formation rate mainly limited by gas dissolution in the liquid phase to a hydrate formation rate mainly limited by hydrate growth in the liquid phase. The position of the representative point of the system for the highest ε_m, next to point "C," represents a situation in which the hydrate formation rate is almost solely dominated by the resistance to heat transfer to the environment. Last, for the Dispersimax, the position of the representative point of the system for the lowest ε_m, close to point "B," depicts a situation in which the hydrate formation rate is mainly limited by hydrate growth in the liquid phase but also, to a lesser extent, by both gas dissolution in the liquid phase and heat transfer to the environment (as this point is also close to point "A" and "C"). The positions of the representative points of the system for higher values of ε_m, next to point "C," represent a situation in which the hydrate formation rate is almost solely dominated by the resistance to heat transfer to the environment.

Conclusion

CO_2 hydrate formation experiments were performed under different flow conditions in a 20 L semi-batch stirred tank reactor of standard geometry in order to examine the impact of the flow conditions on the CO_2 hydrate formation rate. Different flow conditions were generated using three different impellers (a down-pumping pitched blade turbine (PBTD), a Maxblend, and a Dispersimax) at different rotational speeds. Two methods were used to determine the rate-limiting step of the CO_2 hydrate formation process during a given experiment. The first method uses an original mathematical model of the complete CO_2 hydrate formation process that assigns a resistance to each of its steps (gas dissolution in the liquid phase, hydrate growth in the liquid phase, and heat transfer to the environment). It is based on the experimental evaluation, and comparison of the values of these resistances. The second method is based on the determination of the temperature-concentration position of the bulk of the liquid phase during a hydrate formation experiment in the relevant isobaric CO_2-in-water solubility diagram.

For the three impellers used in this study, it was shown that the increase of the mixing intensity, through its decreasing effect on all the resistances involved in the hydrate formation process, resulted in an increase of the formation rate. The capacity of the Maxblend and the Dispersimax to provide high levels of gas-liquid contact and of solid suspension allowed the mass transfer resistances to be substantially decreased, which ultimately led to, at high mixing intensity, in their respective range of mixing intensity studied, a formation rate limited by the heat exchange with the environment. While the range of mixing intensity at which the PBTD was used was similar than the one used for the other two impellers, it did not allow producing such conditions, which was found to be due to its poor ability to provide high levels of gas entrainment in the liquid.

Of the three impellers used in this study, the Maxblend displays by far the best energy performance. For reasons that remain to be clarified, this unusual impeller generates flow conditions that are extremely efficient for the formation of CO_2 hydrates in a stirred tank, compared with other impellers. High pumping capacity, very uniform shear field, and good gas-liquid contact ability can be suspected to be at the origin of this performance since they were demonstrated to be a characteristic of the impeller.[45,47,48] As for the two other impellers, the Dispersimax performed better than the PBTD due its gas induction capability.

In addition to the results related to the impact of flow conditions on the CO_2 hydrate formation rate, the present study also showed that heat transfer limitations occurs at the relatively small scale used to perform our CO_2 hydrate formation experiments. This fact, which is not often reported in the literature, is an important finding for the development of scaling-up strategies for hydrate-based gas separation processes. It is clear that these strategies will have to take into account the transfer of the important heat released by the hydrate formation, even at small scales, by the development of adequate heat exchangers.

Finally, the mathematical model of the CO_2 hydrate formation process and the two methods for determining the rate-limiting steps can be used to design and optimize future industrial-scale gas hydrate formation reactors.

Acknowledgments

The financial support of the National Sciences and Engineering Research Council of Canada (NSERC) and the Federation Wallonia-Brussels (FW-B) is gratefully acknowledged.

Literature Cited

1. Leung DYC, Caramanna G, Maroto-Valer MM. An overview of current status of carbon dioxide capture and storage technologies. *Renewable Sustainable Energ Rev*. 2014;39(C):426–443.
2. Metz B, Davidson O, De Coninck H, Loos M, Meyer L. IPCC, 2005: IPCC special report on carbon dioxide capture and storage. Prepared by Working Group III of the Intergovernmental Panel on Climate Change. Cambridge, United Kingdom and New York, NY, USA: Cambridge University Press; 2005.
3. Eslamimanesh A, Mohammadi AH, Richon D, Naidoo P, Ramjugernath D. Application of gas hydrate formation in separation processes: a review of experimental studies. *J Chem Thermody*. 2012;46(C):62–71.
4. Xu C-G, Li X-S. Research progress of hydrate-based CO_2 separation and capture from gas mixtures. *RSC Adv*. 2014;4(35):18301.
5. Fan S, Li S, Wang J, Lang X, Wang Y. Efficient capture of CO_2 from simulated flue gas by formation of TBAB or TBAF semiclathrate hydrates. *Energy Fuels*. 2009;23(8):4202–4208.
6. Aaron D, Tsouris C. Separation of CO_2 from flue gas: a review. *Sep Sci Technol*. 2005;40(1):321–348.
7. Yang D, Le LA, Martinez RJ, Currier RP, Spencer DF. Kinetics of CO_2 hydrate formation in a continuous flow reactor. *Chem Eng J*. 2011;172(1):144–157.
8. Sloan ED, Koh CA. *Clathrate Hydrates of Natural Gases*, 3rd ed. Boca Raton, FL: CRC Press/Taylor & Francis, 2008.

9. Sloan ED. Fundamental principles and applications of natural gas hydrates. *Nature*. 2003;426(6964):353–363.
10. Englezos P, Kalogerakis N, Dholabhai P, Bishnoi P. Kinetics of formation of methane and ethane gas hydrates. *Chem Eng Sci*. 1987; 42(11):2647–2658.
11. Wang Y, Lang X, Fan S. Hydrate capture CO_2 from shifted synthesis gas, flue gas and sour natural gas or biogas. *J Energy Chem*. 2013;22(1):39–47.
12. Babu P, Linga P, Kumar R, Englezos P. A review of the hydrate based gas separation (HBGS) process for carbon dioxide precombustion capture. *Energy*. 2015;85:261–279.
13. Yang D, Le LA, Martinez RJ, Currier RP, Spencer DF, Deppe G. Heat transfer during CO_2 hydrate formation in a continuous flow reactor. *Energy Fuels*. 2008;22(4):2649–2659.
14. Englezos P, Lee JD. Gas hydrates: a cleaner source of energy and opportunity for innovative technologies. *Korean J Chem Eng*. 2005; 22(5):671–681.
15. Lee S, Liang L, Riestenberg D, West OR, Tsouris C, Adams E. CO_2 hydrate composite for ocean carbon sequestration. *Environ Sci Technol*. 2003;37(16):3701–3708.
16. Hashemi S, Macchi A, Bergeron S, Servio P. Prediction of methane and carbon dioxide solubility in water in the presence of hydrate. *Fluid Phase Equilib*. 2006;246(1-2):131–136.
17. Valtz A, Chapoy A, Coquelet C, Paricaud P, Richon D. Vapour–liquid equilibria in the carbon dioxide–water system, measurement and modelling from 278.2 to 318.2K. *Fluid Phase Equilib*. 2004;226: 333–344.
18. Kang S-P, Lee H. Recovery of CO_2 from flue gas using gas hydrate: thermodynamic verification through phase equilibrium measurements. *Environ Sci Technol*. 2000;34(20):4397–4400.
19. Bergeron S, Servio P. CO_2 and CH_4 mole fraction measurements during hydrate growth in a semi-batch stirred tank reactor and its significance to kinetic modeling. *Fluid Phase Equilib*. 2009;276(2): 150–155.
20. Bergeron S, Servio P. Reaction rate constant of CO_2 hydrate formation and verification of old premises pertaining to hydrate growth kinetics. *AIChE J*. 2008;54(11):2964–2970.
21. Clarke M, Bishnoi P. Determination of the intrinsic kinetics of CO_2 gas hydrate formation using in situ particle size analysis. *Chem Eng Sci*. 2005;60(3):695–709.
22. Ribeiro CP Jr, Lage PLC. Modelling of hydrate formation kinetics: state-of-the-art and future directions. *Chem Eng Sci*. 2008;63(8): 2007–2034.
23. Li X-S, Xu C-G, Chen Z-Y, Wu H-J. Hydrate-based pre-combustion carbon dioxide capture process in the system with tetra-n-butyl ammonium bromide solution in the presence of cyclopentane. *Energy*. 2011;36(3):1394–1403.
24. Seo Y-T, Kang S-P, Lee S, Lee H. Experimental measurements of hydrate phase equilibria for carbon dioxide in the presence of THF, Propylene Oxide, and 1,4-Dioxane. *J Chem Eng Data*. 2008;53(12): 2833–2837.
25. Torré J-P, Dicharry C, Ricaurte M, Daniel-David D, Broseta D. CO_2 capture by hydrate formation in quiescent conditions: in search of efficient kinetic additives. *Energy Procedia*. 2011;4(C):621–628.
26. Mooijer-van den Heuvel MM, Witteman R, Peters CJ. Phase behaviour of gas hydrates of carbon dioxide in the presence of tetrahydropyran, cyclobutanone, cyclohexane and methylcyclohexane. *Fluid Phase Equilib*. 2001;182(1-2):97–110.
27. Kumar A, Sakpal T, Linga P, Kumar R. Influence of contact medium and surfactants on carbon dioxide clathrate hydrate kinetics. *Fuel*. 2013;105:664–671.
28. Lang X, Fan S, Wang Y. Intensification of methane and hydrogen storage in clathrate hydrate and future prospect. *J Natural Gas Chem*. 2010;19(3):203–209.
29. Mori Y. Recent advances in hydrate-based technologies for natural gas storage—a review. *J Chem Ind Eng*. 2003;54:1–17.
30. Linga P, Kumar R, Lee JD, Ripmeester JA, Englezos P. A new apparatus to enhance the rate of gas hydrate formation: application to capture of carbon dioxide. *Intl J Greenhouse Gas Control*. 2010; 4(4):630–637.
31. Hashemi S, Macchi A, Servio P. Gas–liquid mass transfer in a slurry bubble column operated at gas hydrate forming conditions. *Chem Eng Sci*. 2009;64(16):3709–3716.
32. Xu C-G, Cai J, Li X-S, Lv Q-N, Chen Z-Y, Deng H-W. Integrated process study on hydrate-based carbon dioxide separation from integrated gasification combined cycle (IGCC) synthesis gas in scaled-up equipment. *Energy Fuels*. 2012;26(10):6442–6448.
33. Rossi F, Filipponi M, Castellani B. Investigation on a novel reactor for gas hydrate production. *Appl Energy*. 2012;99(C):167–172.
34. Hao W, Wang J, Fan S, Hao W. Study on methane hydration process in a semi-continuous stirred tank reactor. *Energy Conversion Manage*. 2007;48(3):954–960.
35. Szymcek P, McCallum SD, Taboada-Serrano P, Tsouris C. A pilot-scale continuous-jet hydrate reactor. *Chem Eng J*. 2008;135(1-2):71–77.
36. Vysniauskas A, Bishnoi PR. A kinetic study of methane hydrate formation. *Chem Eng Sci*. 1983;38(7):1061–1072.
37. Ke W, Svartaas TM. Effects of stirring and cooling on methane hydrate formation in a high-pressure isochoric cell. In: *Proceedings of the 7th International Conference on Gas Hydrates (ICGH 2011)*, July 2011, Edimburgh.
38. He Y, Rudolph ESJ, Zitha PLJ, Golombok M. Kinetics of and methane hydrate formation: an experimental analysis in the bulk phase. *Fuel*. 2011;90(1):272–279.
39. Mork M, Gudmundsson JS. Hydrate formation rate in a continuous stirred tank reactor: experimental results and Bubble-to-Crystal model. In: *4th International Conference on Gas Hydrates*, June 2002, Yokohama.
40. Happel J, Hnatow MA, Meyer H. The study of separation of sitrogen from methane by hydrate formation using a novel apparatus. *Ann NY Acad Sci*. 1994;715(1):412–424.
41. Ni L, Jingde Z. Characteristics of CO_2 hydrate production with mechanical enhancement. In: *2011 International Conference on Computer Distributed Control and Intelligent Environmental Monitoring (CDCIEM)*, 2011, Changsha.
42. Paul E, Atiemo-Obeng VA, Kresta SM. *Handbook of Industrial Mixing: Science and Practice*. Hoboken, N.J.: Wiley-IEEE, 2004.
43. Fradette L, Thomé G, Tanguy PA, Takenaka K. Power and mixing time study involving a Maxblend® impeller with viscous newtonian and non-newtonian fluids. *Chem Eng Res Design*. 2007;85(11):1514–1523.
44. Hidalgo-Millán A, Zenit R, Palacios C, et al. On the hydrodynamics characterization of the straight Maxblend® impeller with Newtonian fluids. *Chem Eng Res Design*. 2012;90(9):1117–1128.
45. Guntzburger Y, Fontaine A, Fradette L, Bertrand F. An experimental method to evaluate global pumping in a mixing system: application to the Maxblend™ for Newtonian and non-Newtonian fluids. *Chem Eng J*. 2013;214(C):394–406.
46. Dohi N, Takahashi T, Minekawa K, Kawase Y. Power consumption and solid suspension performance of large-scale impellers in gas–liquid–solid three-phase stirred tank reactors. *Chem Eng J*. 2004;97(2-3):103–114.
47. Stobiac V, Fradette L, Tanguy PA, Bertrand F. Pumping characterisation of the maxblend impeller for Newtonian and strongly non-Newtonian fluids. *Can J Chem Eng*. 2014;92(4):729–741.
48. Yatomi R, Takenaka K, Takahashi K, Tanguy PA. Mass-transfer characteristics by surface aeration of large paddle impeller: application to a polymerization reactor with liquid level change. *Chem Eng Res Design*. 2008;86(12):1345–1349.
49. Armenante PM, Nagamine EU. Effect of low off-bottom impeller clearance on the minimum agitation speed for complete suspension of solids in stirred tanks. *Chem Eng Sci*. 1997;53(9):1757–1775.
50. Bishnoi PR, Natarajan V. Formation and decomposition of gas hydrates. *Fluid Phase Equilib*. 1996;117(1-2):168–177.
51. Diamond LW, Akinfiev NN. Solubility of CO_2 in water from -1.5 to 100°C and from 0.1 to 100 MPa: evaluation of literature data and thermodynamic modelling. *Fluid Phase Equilib*. 2003;208(1-2):265–290.
52. Malegaonkar M, Dholabhai P, Bishnoi P. Kinetics of carbon dioxide and methane hydrate formation. *Can J Chem Eng*. 1997;75(6):1090–1099.
53. Sharratt PN. *Handbook of Batch Process Design*. Dordrecht: Springer, 1997.
54. Hashemi S, Macchi A, Servio P. Gas hydrate growth model in a semibatch stirred tank reactor. *Ind. Eng. Chem. Res*. 2007;46(18): 5907–5912.
55. Mullin JW. *Crystallization*, 4th ed. Oxford: Elsevier Butterworth-Heinemann, 2001.
56. Bird RB, Stewart WE, Lightfoot EN. *Transport Phenomena*, New York: Wiley, 2007.
57. Matsuoka M, Garside J. Non-isothermal effectiveness factors and the role of heat transfer in crystal growth from solutions and melts. *Chem Eng Sci*. 1991;46(1):183–192.

58. Delahaye A, Fournaison L, Marinhas S, et al. Effect of THF on equilibrium pressure and dissociation enthalpy of CO2 hydrates applied to secondary refrigeration. *Ind Eng Chem Res*. 2006;45(1):391–397.
59. Beenackers AACM, Van Swaaij WPM. Mass transfer in gas—liquid slurry reactors. *Chem Eng Sci*. 2001;48(18):3109–3139.
60. Moucha T, Linek V, Prokopová E. Gas hold-up, mixing time and gas–liquid volumetric mass transfer coefficient of various multiple-impeller configurations: rushton turbine, pitched blade and techmix impeller and their combinations. *Chem Eng Sci*. 2003;58(9):1839–1846.
61. Genck WJ. Optimizing crystallizer scaleup. *Chem Eng Prog*. 2003; 99(6):36–36.
62. Bhattacharya S, Hebert D, Kresta SM. Air entrainment in baffled stirred tanks. *Chem Eng Res Design*. 2007;85(5):654–664.
63. Martinez MC, Dalmazzone D, Furst W, Delahaye A, Fournaison L. Thermodynamic properties of THF + CO_2 hydrates in relation with refrigeration applications. *AIChE J*. 2008;54(4):1088–1095.

Manuscript received Feb. 18, 2015, and revision received May 31, 2015.